Supplementary Information

Emergent Disorder Screening in Ag–Zn Co-doped Magnetic MnTe Thermoelectrics: Carrier Concentration–Stabilized Mobility for Enhanced Electronic Transport

Sri Sai Samhitha Gadhavajhala‡, Srivathsan Prakasam‡, Veera Prabu Kannan*, Gang Bahadur Acharya, Bhuvanesh Srinivasan*

Thermal Energy Materials Group, Department of Metallurgical and Materials Engineering, Indian Institute of Technology Madras, Chennai 600 036, India

*Email: gruprabu@gmail.com; bhuvanesh.srini@iitm.ac.in

‡ Authors contributed equally and share the first authorship

X-Ray Diffraction (XRD)

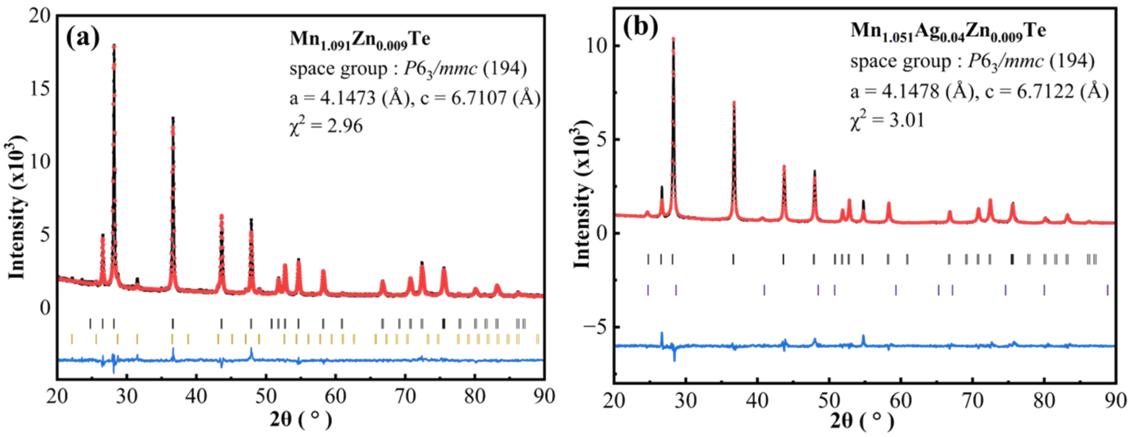

Figure S1. *Refinement plots (a) $Mn_{1.091}Zn_{0.009}Te$, (b) $Mn_{1.051}Ag_{0.04}Zn_{0.009}Te$. The experimental XRD patterns are indicated in red circular symbol, the refined XRD pattern is indicated in black line, while the difference between the refined and experimental XRD pattern is indicated in blue line, and vertical ticks indicate the standard XRD pattern of MnTe (black), $MnTe_2$ (Chinese gold) and ZnTe (purple).*

Table S1. *Rietveld refined parameters (a, c), phase fractions, and goodness of fit (χ^2) of $Mn_{1.1}Te$, $Mn_{1.091}Zn_{0.009}Te$, $Mn_{1.071}Ag_{0.02}Zn_{0.009}Te$, and $Mn_{1.051}Ag_{0.04}Zn_{0.009}Te$, samples.*

Parameters	**Crystal structure: NiAs-type hexagonal ($P6_3/mmc$)**			
	$Mn_{1.1}Te$	**$Mn_{1.091}Zn_{0.009}Te$**	**$Mn_{1.071}Ag_{0.02}Zn_{0.009}Te$**	**$Mn_{1.051}Ag_{0.04}Zn_{0.009}Te$**
a (Å)	4.14485	4.14732	4.14781	4.41784
c (Å)	6.70592	6.71018	6.71186	6.71213
MnTe (vol%)	95.03	96.59	98	95.1
$MnTe_2$ (vol%)	4.97	3.41	-	-
ZnTe (vol%)	-	-	2	2.2
Ag_2Te	-	-	-	2.7

χ^2	2.87	2.96	3.62	3.1

Scanning Electron Microscope (SEM)

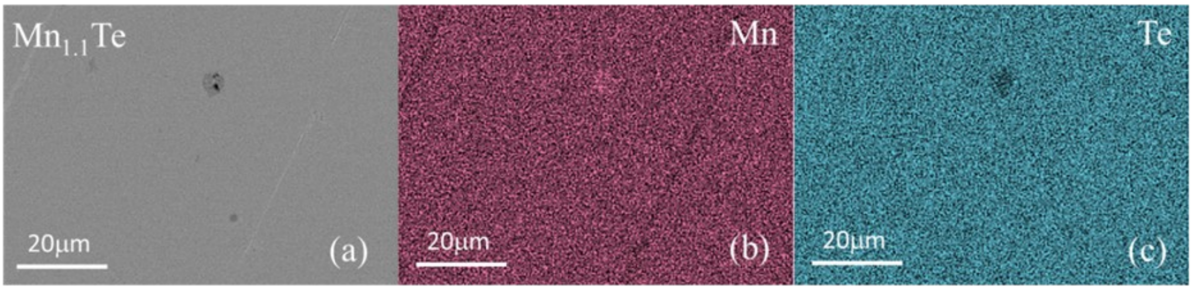

Figure S2. *SEM image of (a)* $Mn_{1.1}Te$ *and its EDS mapping of (b) Mn and (c) Te elements.*

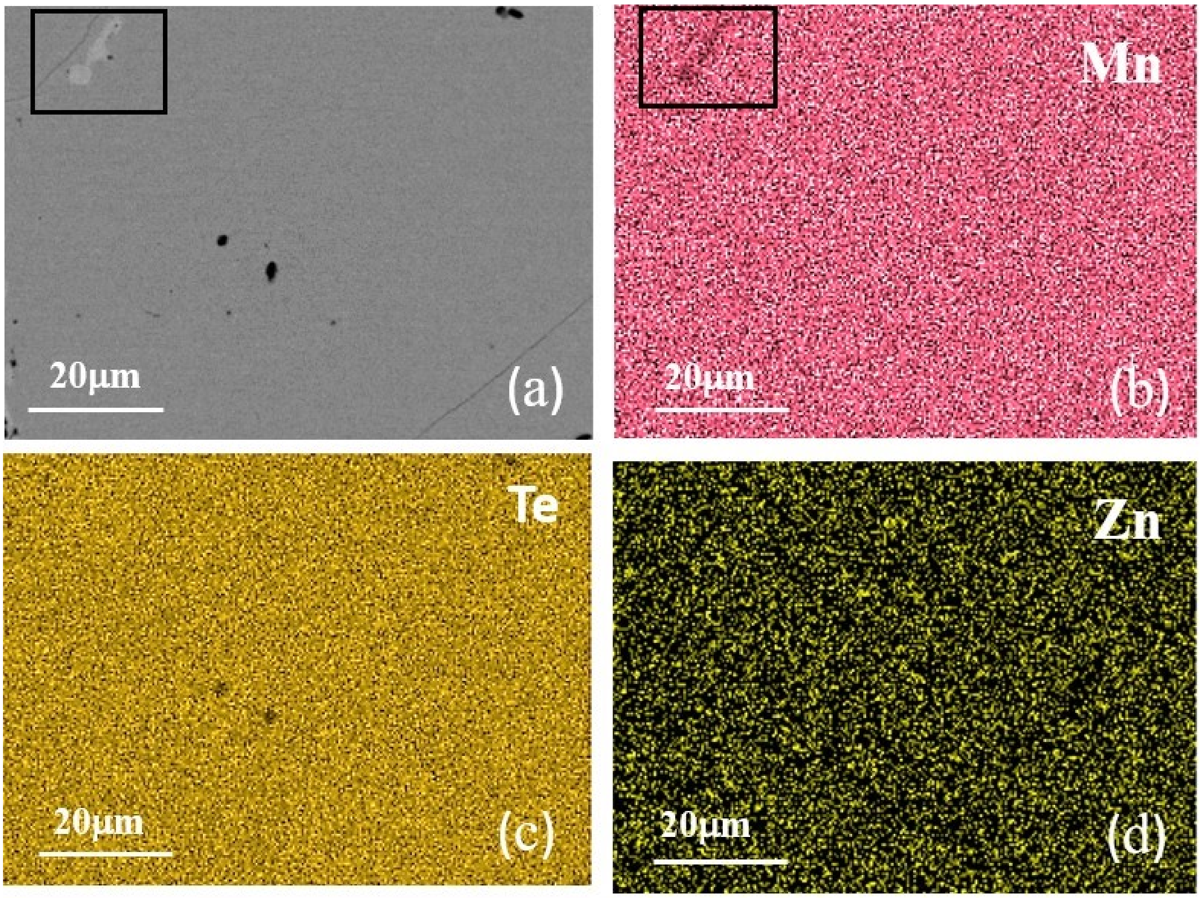

Figure S3. *SEM image of (a)* $Mn_{1.091}Zn_{0.009}Te$ *and its EDS mapping of (b) Mn, (c) Te, (d) Zn elements.*

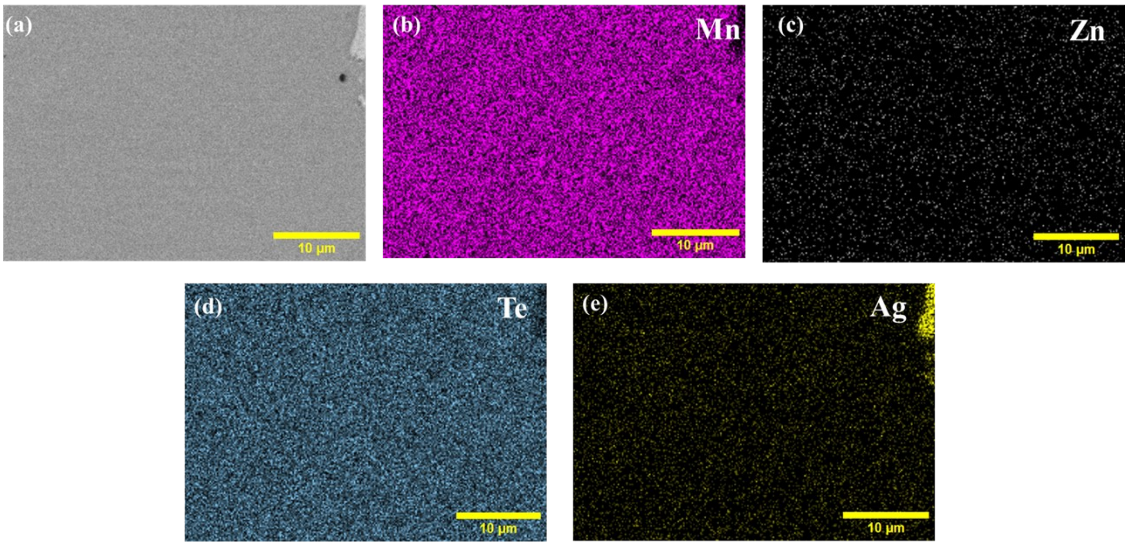

Figure S4. *SEM image of (a)* $Mn_{1.071}Ag_{0.02}Zn_{0.009}Te$ *and its EDS mapping of (b) Ag, (c) Zn, (d) Mn and (e) Te elements.*

Differential Scanning Colorimetry (DSC)

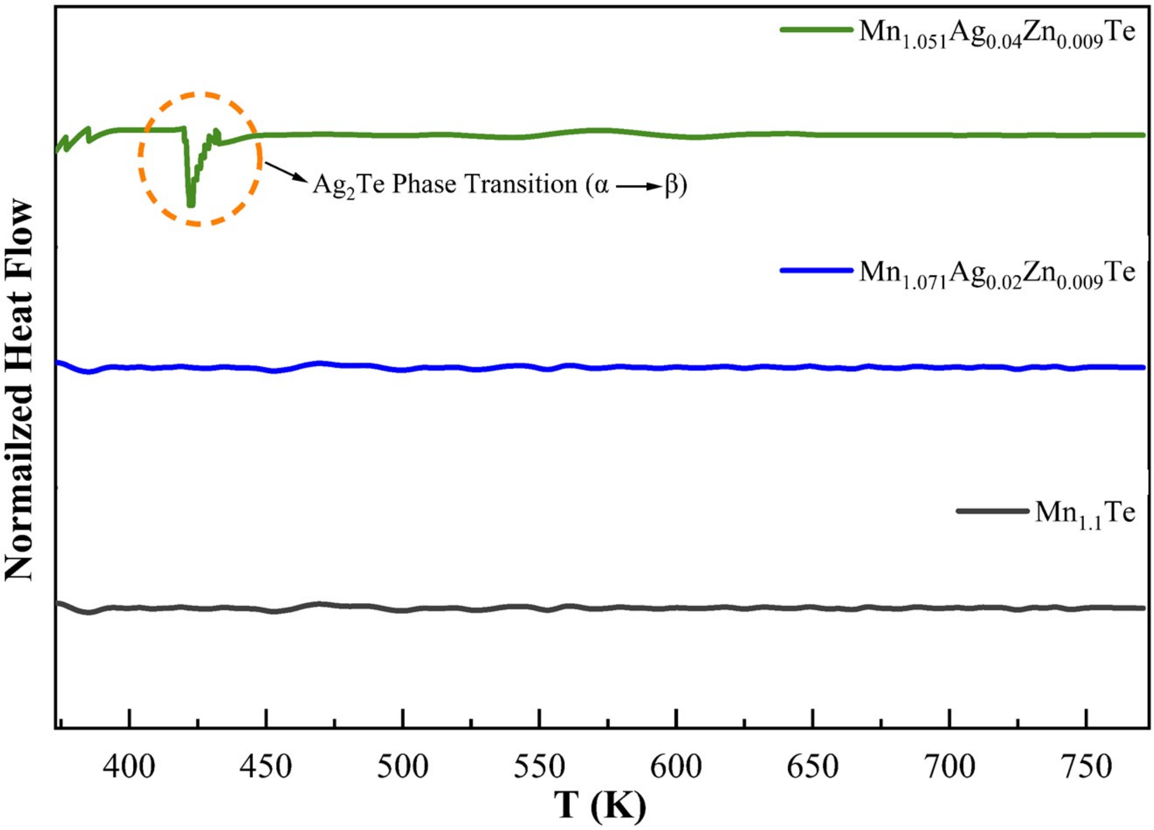

Figure S5*. Differential scanning calorimetry (DSC) curve of* $Mn_{1.1}Te$, $Mn_{1.071}Ag_{0.02}Zn_{0.009}Te$ *and* $Mn_{1.051}Ag_{0.04}Zn_{0.009}Te$ *samples. All the samples show good thermal stability. While the endothermic peak observed at approximately 423 K in the* $Mn_{1.051}Ag_{0.04}Zn_{0.009}Te$ *sample is* *attributed to the characteristic* α-Ag_2Te *to* β-Ag_2Te *phase transition.*[1] *The phase transition from* α-Ag_2Te *to* β-Ag_2Te *is not associated with spin-phonon coupling in the sample occurring in the antiferromagnetic region.*

Potential Seebeck Microprobe (PSM)

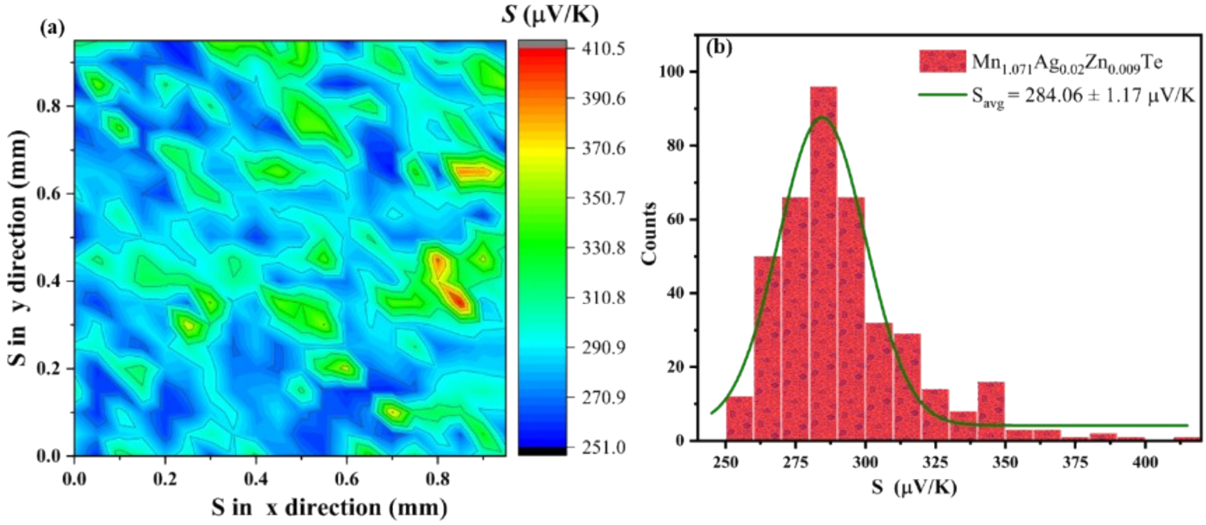

Figure S6. *(a) Spatial mapping of the Seebeck coefficient across the surface of* $Mn_{1.071}Ag_{0.02}Zn_{0.009}Te$ *using a Potential Seebeck Microprobe, and (b) the corresponding histogram showing the homogeneous distribution of Seebeck coefficient values.*

To examine chemical homogeneity and the possible effect of secondary phases on the Seebeck coefficient, Seebeck microprobe analysis was performed using a Potential Seebeck Microprobe (PSM II). Seebeck mapping of the $Mn_{1.071}Ag_{0.02}Zn_{0.009}Te$ sample was carried out over an area of 1 mm × 1 mm with a spatial resolution of 50 μm. As shown in Figure S6a, most regions display blue and green colours, corresponding to the Seebeck coefficient of the $Mn_{1.071}Ag_{0.02}Zn_{0.009}Te$ matrix. These values agree well with the bulk measurements obtained using the ZEM-3 system. A few isolated red and yellow regions are observed, which may arise from minor secondary phases, surface oxidation, or surface porosity. Overall, the Seebeck mapping confirms good chemical homogeneity of the $Mn_{1.071}Ag_{0.02}Zn_{0.009}Te$ sample. The Seebeck coefficient distribution shown in Figure S6b gives an average value of 284.06 ± 1.17 $\mu V\ K^{-1}$, consistent with the ZEM-3 results.

UV-Vis Spectroscopy

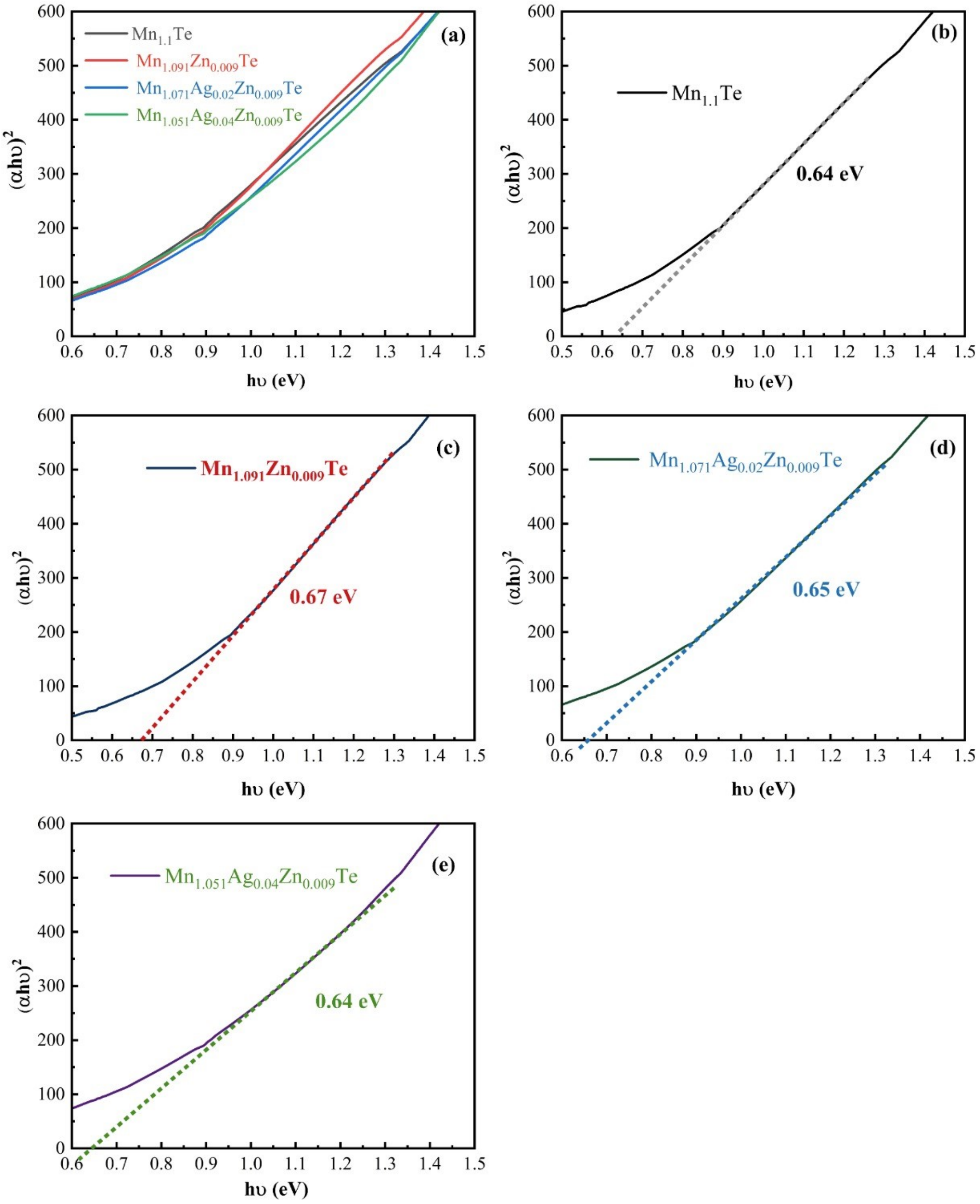

Figure S7. *Tauc plot obtained from UV-Vis spectroscopy to estimate band gap (a) combined plot for all the compositions (b)* $Mn_{1.1}Te$ *(c)* $Mn_{1.091}Zn_{0.009}Te$ *(d)* $Mn_{1.071}Ag_{0.02}Zn_{0.009}Te$ *and (e)* $Mn_{1.051}Ag_{0.04}Zn_{0.009}Te$*.*

To understand the changes in the band gap induced by co-doping in MnTe, UV-Vis-NIR spectroscopy was performed on the co-doped samples to estimate the optical band gap. Tauc plots of $(\alpha h\nu)^2$ versus $h\nu$ were constructed, and the band gap values were determined by extrapolating the linear region to the energy axis, where the intercept gives the band gap in eV. The estimated band gap values are 0.64 eV for $Mn_{1.1}Te$, 0.67 eV for $Mn_{1.091}Zn_{0.009}Te$, 0.65 eV for $Mn_{1.071}Ag_{0.02}Zn_{0.009}Te$, and 0.64 eV for $Mn_{1.051}Ag_{0.04}Zn_{0.009}Te$, respectively.

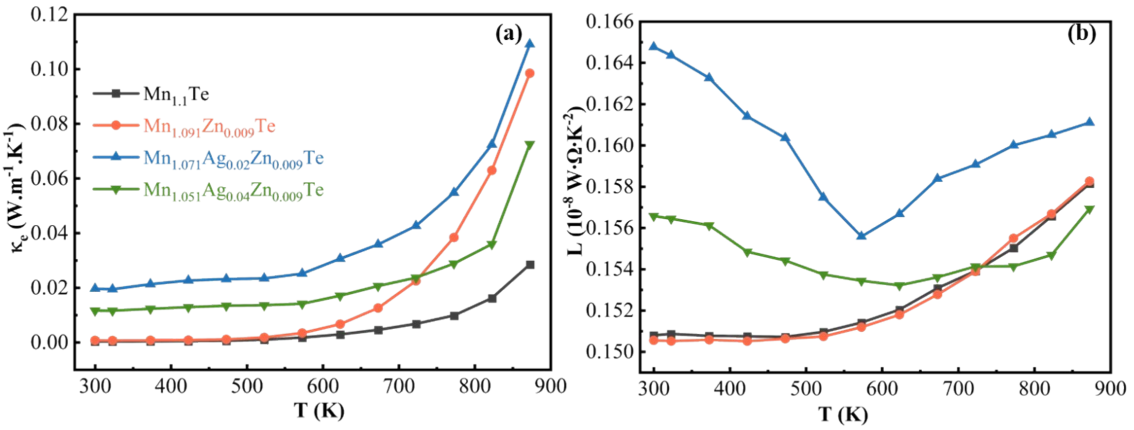

Thermal Transport Properties

Figure S8. *Temperature-dependent (a) electronic thermal conductivity and (b) Lorenz number for* $Mn_{1.1}Te$, $Mn_{1.091}Zn_{0.009}Te$, $Mn_{1.071}Ag_{0.02}Zn_{0.009}Te$, *and* $Mn_{1.051}Ag_{0.04}Zn_{0.009}Te$ *samples.*

The Figure S8 shows the temperature-dependent variation of (a) Lorenz number and (b) electronic thermal conductivity for all the compositions. Total thermal conductivity for all the compositions was calculated using the relation:[2]

$$\kappa_T = D \times C_p \times \rho \tag{SE1}$$

Here, ρ represents the density, determined using Archimedes' principle, D is the thermal diffusivity, and C_p is the specific heat capacity, estimated from the Dulong-Petit law. The density values for $Mn_{1.1}Te$, $Mn_{1.091}Zn_{0.009}Te$, $Mn_{1.071}Ag_{0.02}Zn_{0.009}Te$, and $Mn_{1.051}Ag_{0.04}Zn_{0.009}Te$ are 6.00, 5.98, 5.98, 5.97 g/cc respectively.

The electronic thermal conductivity of all compositions was estimated using the following relation,

$$\kappa_e = L \times \sigma \times T \tag{SE2}$$

where L is the Lorenz number calculated assuming Single Parabolic Band (SPB) model,[2]

$$L = 1.5 + \exp\left(-\frac{|S|}{116}\right) \times 10^{-8} \tag{SE3}$$

where S is the Seebeck coefficient.

The theoretical minimum thermal conductivity of the MnTe compounds was calculated using the following relation,[3]

$$\kappa_{L,min} = 1.21\, n^{2/3} k_B \left(\frac{1}{3}\right)(2v_T + v_L) \tag{SE4}$$

where n is the number of atoms, k_B is the Boltzmann constant, v_L and v_T are the longitudinal and transverse sound velocities.

Strain and Mass Fluctuations

Total disorder scattering parameter (Γ) was calculated, which is a sum ($\Gamma = \Gamma_{MF} + \Gamma_{SF}$) of strain field ($\Gamma_{SF}$) and mass fluctuations (Γ_{MF}) , which were estimated using the following equations:[4,5]

$$\Gamma_{MF} = \frac{n_{sublattice}}{n_{compound}}\left(\frac{\bar{M}_{sublattic}}{M_{compound}}\right) x(1-x)\left(\frac{M_1 - M_2}{\bar{M}_{sublattice}}\right)^2 \quad \text{(SE5)}$$

$$\Gamma_{SF} = \frac{n_{sublattice}}{n_{compound}}\left(\frac{\bar{M}_{sublattic}}{M_{compound}}\right) x(1-x)\varepsilon\left(\frac{R_1 - R_2}{\bar{R}_{sublattice}}\right)^2 \quad \text{(SE6)}$$

$n_{sublattice}$ and $n_{compound}$ are the sublattice and the total occupancy (for $Mn_{1.1}Te$, $n_{sublattice} =$ 1 and $n_{compound} = 2$). M_i and R_i represent the atomic mass and radius of atoms (Mn, Zn /Ag-Zn), $\bar{M}_{sublattic}$ and $\bar{R}_{sublattic}$ are average atomic mass and average atomic radius for the sublattice (Mn, Zn /Ag-Zn) , $M_{compound}$ is the average atomic mass of samples, x is the fractional atomic concentration of dopants (Zn /Ag-Zn). ε is the phenomenological adjustable parameter.

The phenomenological adjustable parameter ε was calculated using the following relation,[6]

$$\varepsilon = \frac{2}{9}\left(\frac{6.4 \times \gamma(1+v_p)}{(1-v_p)}\right)^2 \quad \text{(SE7)}$$

where v_p is the Poisson's ratio and γ is the Grüneisen parameter.

Debye-Callaway Model

The significant reduction in lattice thermal conductivity observed in the $Mn_{1.071}Ag_{0.02}Zn_{0.009}Te$ sample was examined using the Debye–Callaway model to quantify the contributions of the various phonon-scattering processes. The spectral lattice thermal conductivity was calculated using the following relation,[4]

$$\kappa_S = \frac{k_B}{2\pi^2 v_s}\left(\frac{k_B T}{\hbar}\right)^3 \int x^4 \tau(x) \frac{e^x}{(e^x - 1)^2} dx \quad \text{(SE8)}$$

where k_B is the Boltzmann constant, $\hbar$ is the reduced Planck's constant, v_s is the average sound velocity, T is the temperature, x is the reduced phonon frequency ($x = \frac{\hbar\omega}{k_B T}$: where ω is the phonon frequency), and $\tau(x)$ is the total phonon relaxation time.

The total phonon scattering rate was obtained by combining the relaxation times associated with individual scattering processes, including Umklapp, grain-boundary, point-defect, and dislocation strain scattering, according to the following relation,[7]

$$\tau^{-1}(x) = \tau_U^{-1}(x) + \tau_{PD}^{-1}(x) + \tau_{GD}^{-1}(x) + \tau_D^{-1}(x) \tag{SE9}$$

$\tau_U^{-1}(x)$ corresponds to Umklapp scattering, which arises due to the three-phonon interactions and is calculated using the following relation,[7]

$$\tau_U^{-1}(x) = \frac{k_B^2 \gamma^2}{\hbar M v_s^2 \theta_a} x^2 T^3 e^{-\theta_a/3T} \tag{SE10}$$

where $\theta_a = \frac{\theta_D}{n^{1/3}}$ is the acoustic Debye temperature (θ_D = is the Debye temperature and n = is the number of atoms in the unit cell), M is the molecular weight of the formula unit, and γ is the Grüneisen parameter.

$\tau_{GD}^{-1}(x)$ corresponds to scattering of phonons at the grain boundary, which can be calculated using the following relation,[8]

$$\tau_{GD}^{-1}(x) = \frac{v_s}{l} \tag{SE11}$$

where l is the average grain size obtained from the optical microscope.

$\tau_{PD}^{-1}(x)$ corresponds to the scattering of phonons due to point defects, arising from the introduction of dopants in the MnTe system, which is given by,[5]

$$\tau_{PD}^{-1}(x) = \frac{k_B^4 V_{atom} \Gamma}{4\pi \hbar^4 v_s^3} x^4 T^4 \tag{SE12}$$

Where, V_{atom} denotes the average atomic volume of the compound, and Γ represents the disorder scattering parameter, defined as the sum of the mass (Γ_{mass}) and strain (Γ_{strain}) contributions. This disorder originates from differences in atomic size and mass between the host and dopant atoms, which induce lattice distortions and modify the local periodic potential, thereby enhancing phonon scattering and significantly reducing the lattice thermal conductivity.

$\tau_D^{-1}(x)$ corresponds to the scattering of phonons due to dislocations,[9]

$$\tau_D^{-1}(x) = 0.7\left(\frac{k_B T}{\hbar}\right)^2 \frac{a^2\gamma^2 N_{DS}}{v_s} x^2 \tag{SE13}$$

where, a is the lattice parameter and N_{DS} is the number of dislocations crossing a line of unit length.

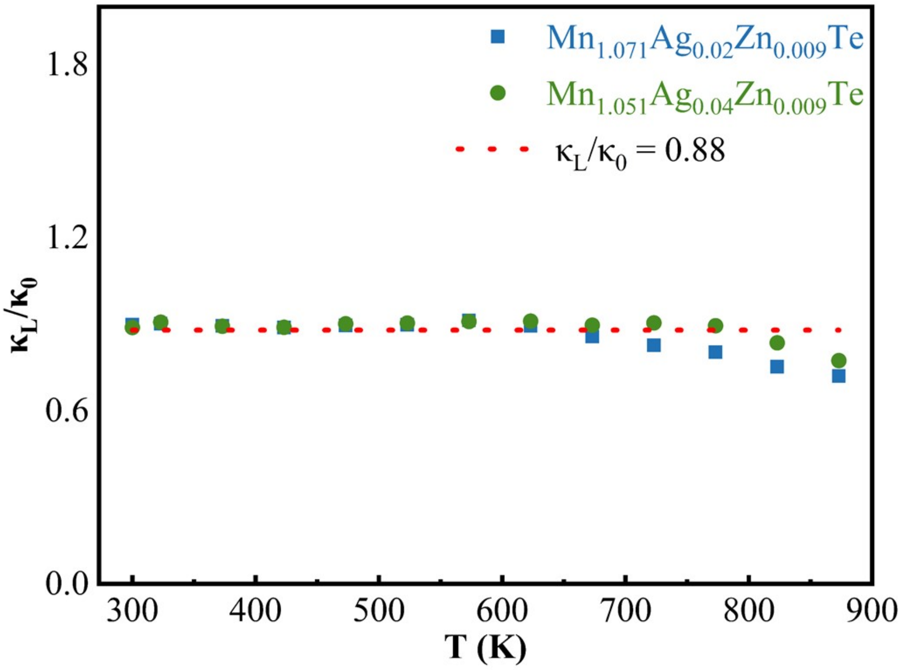

Figure S9. *Normalized lattice thermal conductivity* (κ_L/κ_0) *of* $Mn_{1.071}Ag_{0.02}Zn_{0.009}Te$ *and* $Mn_{1.051}Ag_{0.04}Zn_{0.009}Te$ *with respect to pristine MnTe, where* κ_L*and* κ_0*denote the lattice thermal conductivity of the co-doped samples and pristine MnTe, respectively.*[10] *The nearly constant slope indicates that lattice softening is the dominant mechanism responsible for the reduction in lattice thermal conductivity in the co-doped samples.*

Nanoindentation

The hardness (H) and Young's modulus (E) of the samples were determined from the load–displacement curves obtained from nanoindentation using the following relations,[11]

$$H = \frac{P}{A_p} \tag{SE14}$$

$$E = \frac{\sqrt{\pi}\ S}{2\beta\sqrt{A_p}} \tag{SE15}$$

where P is the load at the indentation depth, A_p is the projected area of the contact surface under the action of P, S is the elastic stiffness constant and β is the indenter constant.

Sound Velocity Measurements

The longitudinal (v_L)and transverse (v_T) sound velocity of the samples were determined using a pulse-echo transducer, using which the average sound velocity (v_s), Young's (E) , bulk (B) and shear (G) modulus were calculated according to the following relations.[8]

$$v_s = \left[\frac{1}{3}\left(\frac{2}{v_t^3} + \frac{1}{v_l^3}\right)\right]^{-1/3} \tag{SE16}$$

$$B = \rho\left(v_L^2 - \frac{4}{3}v_T^2\right) \tag{SE17}$$

$$G = v_T^2\,\rho \tag{SE18}$$

$$E = \frac{9BG}{3B + G} \tag{SE19}$$

Debye temperature (θ_D) for the MnTe compound was estimated using the following relation,[9]

$$\theta_D = \frac{\hbar v_s}{k_B}\left(\frac{6\pi^2 N_A}{V_m}\right)^{1/3} \tag{SE20}$$

where, N_A is the Avogadro number and V_m is the molar volume (m^3.mol^{-3}).

Raman Spectroscopy

Table S2. *Experimental data of Raman frequency (ω), FWHM, and phonon life time (τ) of $Mn_{1.1}Te$, $Mn_{1.091}Zn_{0.009}Te$, $Mn_{1.071}Ag_{0.02}Zn_{0.009}Te$ and $Mn_{1.051}Ag_{0.04}Zn_{0.009}Te$ samples.*

S. No.	Sample	ω (cm^{-1})	FWHM (cm^{-1})	$\tau\ (10^{-14}s)$
1	$Mn_{1.1}Te$	173.86	9.09	58.37
2	$Mn_{1.091}Zn_{0.009}Te$	173.71	10.08	52.65
3	$Mn_{1.071}Ag_{0.02}Zn_{0.009}Te$	173.53	10.29	51.55
4	$Mn_{1.051}Ag_{0.04}Zn_{0.009}Te$	173.23	10.67	49.75

Table S3. *Temperature dependent Raman frequency (ω), FWHM, and phonon lifetime (τ) of $Mn_{1.071}Ag_{0.02}Zn_{0.009}Te$.*

Sl.No.	$Mn_{1.071}Ag_{0.02}Zn_{0.009}Te$	ω (cm^{-1})	FWHM (cm^{-1})	$\tau\ (10^{-14}s)$
1.	283	175.48	10.07	52.68
2.	293	174.42	10.01	52.99
3.	303	174.25	10.15	52.26
4.	313	174.78	9.89	53.62
5.	323	175.09	9.24	57.43

6.	333	174.89	10.02	52.94
7.	343	174.49	10.11	52.47
8.	353	174.26	10.01	52.99
9.	363	174.23	10.17	52.14
10.	373	173.91	10.69	49.61

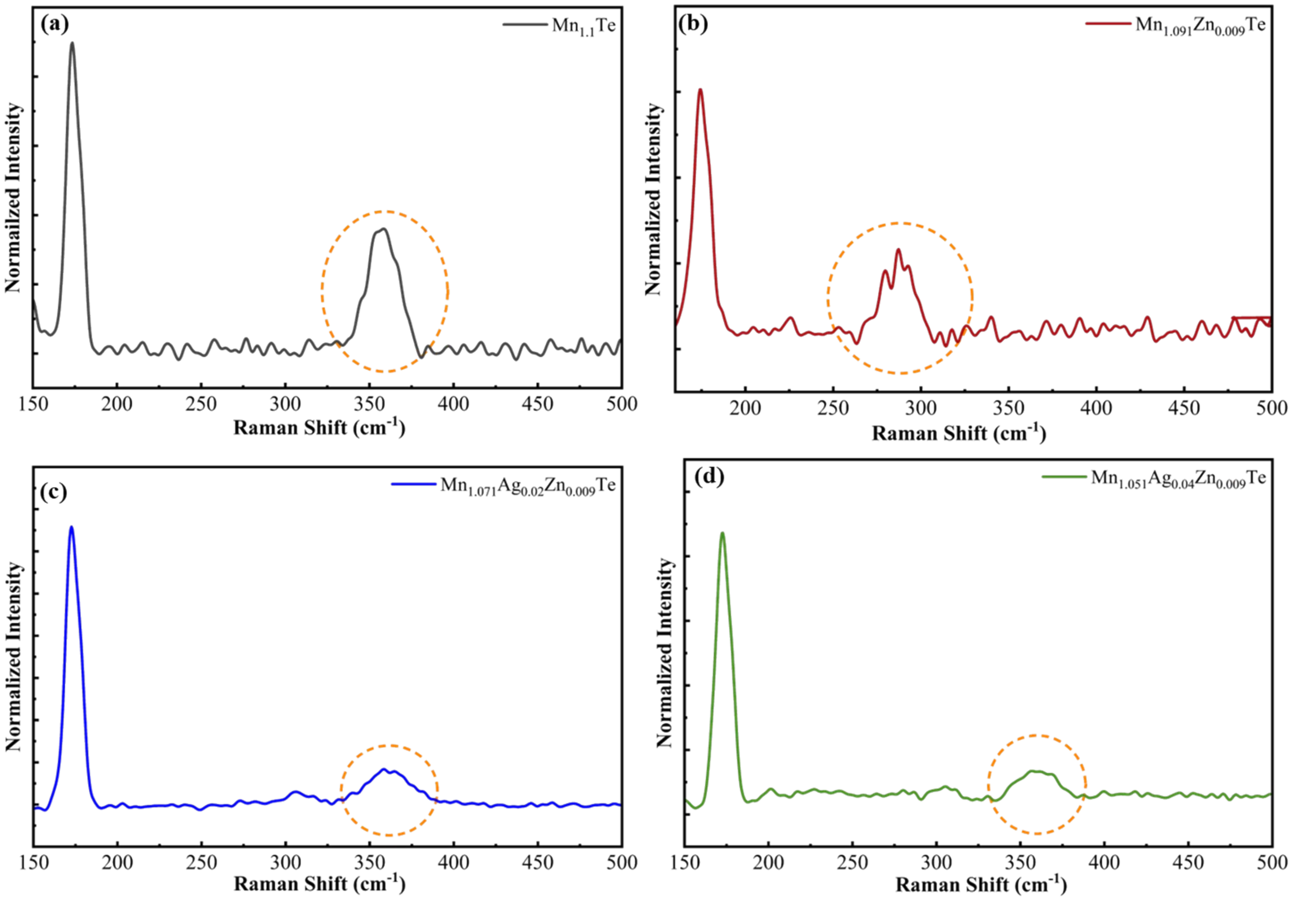

Figure S10: *Room-temperature Raman spectra of (a)* $Mn_{1.1}Te$*, (b)* $Mn_{1.091}Zn_{0.009}Te$*, (c)* $Mn_{1.071}Ag_{0.02}Zn_{0.009}Te$*, and (d)* $Mn_{1.051}Ag_{0.04}Zn_{0.009}Te$ *samples, recorded over the range of 150–500* cm^{-1}*. All samples exhibit the characteristic* E_{2g} *mode of MnTe at ~170–175* cm^{-1}*, along with a magnon peak (highlighted by an orange circle) in the 200–450* cm^{-1} *region.*[12]

Debye Callaway Model Parameters

Table S4. *Parameters used in determining the spectral lattice thermal conductivity of* $Mn_{1.071}Ag_{0.02}Zn_{0.009}Te$ *from the Debye-Callaway Model.*

Parameters	**Values**
Boltzmann Constant ($m^2 \cdot kg \cdot s^{-2} \cdot K^{-1}$)	1.38065×10^{-23}
Grüneisen parameter (γ)	3.5
Planck constant ($m^2 \cdot kg \cdot s^{-1}$)	6.626×10^{-34}
Longitudinal sound velocity (m/s)	3792
Transverse sound velocity (m/s)	1989
Average sound velocity (m/s)	2207
Average mass per atom (kg)	1.495×10^{-25}
Debye temperature θ_D (K)	157.09
Number of atoms per unit cell (n)	4
Temperature (K)	300
Avogadro number (mol^{-1})	6.023×10^{23}
Average grain size (m)	25.13×10^{-6}
Lattice constant, a (Å)	4.1478
Lattice constant, c (Å)	6.7118
Density (kg/m^3)	5987.9
Atomic radius of Mn (pm)	67
Atomic radius of Ag (pm)	115
Atomic radius of Ge (pm)	74
Mass of Mn (g/mol)	54.938
Mass of Ag (g/mol)	107.8682
Mass of Zn (g/mol)	65.38
Mass of Te (g/mol)	127.6
Poisons ratio (v_p)	0.31
Phenomenological adjustable parameter (ε)	546.7278
Number of dislocations per unit length (m^{-1})[9]	6.5×10^5

Density Functional Theory

Methods

First-principles density functional theory (DFT) calculations were performed within the Perdew–Burke–Ernzerhof (PBE) generalized gradient approximation (GGA).[13] Full-potential local-orbital (FPLO) software was used for self-consistent field (SCF), density-of-states, and band-structure calculations.[14] Reciprocal-space integrations were performed using the linear tetrahedron method with Blöchl corrections. A dense 12 × 12 × 12 k-point grid was used to ensure accurate electronic structure analysis. The convergence thresholds were set to 10^{-8} Hartree for energy and 10^{-6} e/(Bohr radii)^3 for charge density. Both scalar-relativistic (without SOC) and fully relativistic (with SOC) calculations were carried out, with the latter involving the solution of the four-component Dirac equation. The GGA+U approach was applied for the Mn atom to treat electronic correlations in the Mn 3d states. The Coulomb interaction parameters were set as F0 = U = 4 eV, F2 = 5.5 eV, and F4 = 8.5 eV, corresponding to a Hund's exchange parameter J = 1 eV.

Magnetic ground state and electronic properties:

To confirm the magnetic ground state of pristine MnTe, ferromagnetic (FM) and antiferromagnetic (AFM) spin-polarized calculations are carried out using the GGA and GGA+U methods. Within GGA, the AFM configuration is found to be more stable, with its energy approximately 0.40 eV lower than that of the FM state. Similarly, within GGA+U, the AFM state remains the ground state, showing an energy difference of approximately 0.22 eV relative to the FM configuration. In the AFM phase, the Mn magnetic moment obtained within GGA is 4.46 µB per atom. When the using GGA+U approach, the moment increases to 4.83 µB per Mn atom. This enhanced value is in good agreement with neutron diffraction measurements, which report Mn magnetic moments in the range 4.7–5 µB.[15] After identifying the AFM configuration as the ground state, the electronic structure is studied by analysing the density of states (DOS) and the electronic band structure.

Figure S10a presents the spin-resolved total and partial DOS of pristine MnTe. The electronic states close to the Fermi level (as 0 eV) mainly consist of Mn-3d orbitals, whereas the Te-5p states are distributed at deeper energies in the range of −5 to −1 eV. A noticeable exchange splitting between the spin-up and spin-down components is observed, which is in agreement with the antiferromagnetic ground state. The absence of electronic states at the Fermi level confirms the semiconducting character of MnTe. Furthermore, the partial density of states reveals significant Mn-3d and Te-5p hybridization, particularly around −5 eV, corresponding to bonding states, and near 3 eV with antibonding states with respect to the Fermi energy. The band structures calculated without and with spin–orbit coupling (SOC) is shown in Figure S10c and Figure S10d, respectively. In the absence of SOC, the top of the valence band exhibits nearly degenerate bands at the Γ point. Upon inclusion of SOC, this degeneracy is lifted, leading to a splitting of the valence-band states. However, the general band topology and the semiconducting character are preserved. This finding is consistent with earlier experimental and theoretical reports on MnTe.[16,17]

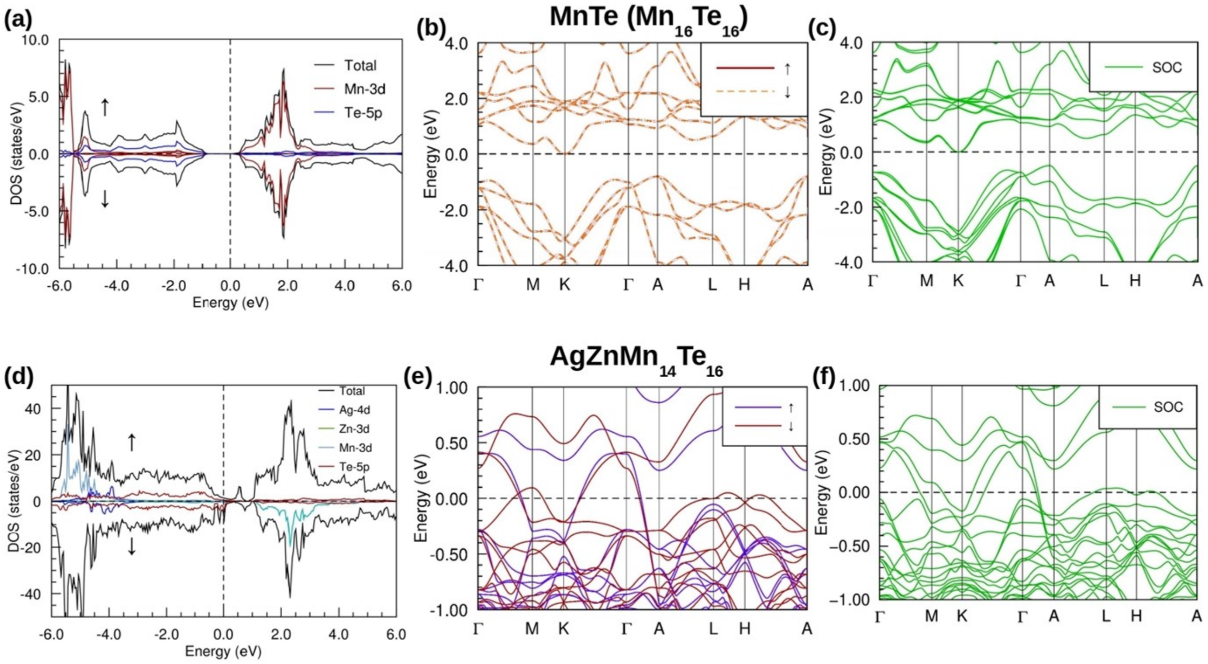

Figure S11: *(a) Spin-polarized total and partial density of states (DOS) of MnTe ($Mn_{16}Te_{16}$). The vertical dashed line denotes the Fermi level, set at 0 eV. The upward and downward arrows represent spin-up and spin-down contributions, respectively. (b) Spin-resolved electronic band structure of $Mn_{16}Te_{16}$ without spin–orbit coupling (SOC) and (c) with SOC. (d) Spin-polarized total and partial DOS of $AgZnMn_{14}Te_{16}$. (e) Spin-polarized electronic band structure of $AgZnMn_{14}Te_{16}$ without SOC and (f) with SOC. In all band-structure plots, the horizontal dashed line indicates the Fermi level.*

Further, to explore the effect of carrier doping, a 2 × 2 × 2 supercell of MnTe was constructed, in which two Mn atoms were substituted with Ag and Zn, yielding $AgZnMn_{14}Te_{16}$. The resulting spin-polarized DOS and band structures are shown in Figure S10d–f.

$AgZnMn_{14}Te_{16}$ shows metallic behaviour, as indicated by a finite density of states at the Fermi level (Figure S10d). Replacing two Mn^{2+} ions with Ag^{+} and Zn^{2+} lowers the total positive charge, which introduces hole doping and partially reduces the Mn-3d states. This hole-doping imbalance shifts the Fermi level into the top of the valence band, which is mainly composed of Te-5p states. The strong interaction between Mn-3d and Te-5p orbitals pushes these states toward the Fermi level, leading to the closure of the band gap. The Zn-3d and Ag-4d states remain localized at lower energies and do not contribute directly at the Fermi level. Figure

S10e shows the electronic band structure calculated without SOC, where bands from both spin channels cross the Fermi level, confirming the metallic nature of the system. Figure S10f shows the band structure with SOC, where the energy bands are split.

Phonon Mean Free Path

The phonon mean free path (l_p) can be calculated using the following equation:[2]

$$\kappa_L = \frac{1}{3} C_v v_s^2 l_p \qquad \text{(SE 21)}$$

where, κ_L is the lattice thermal conductivity of the co-doped sample, C_v is the specific heat at constant volume, and v_s is the average sound velocity of the co-doped sample.

Pisarenko Plot

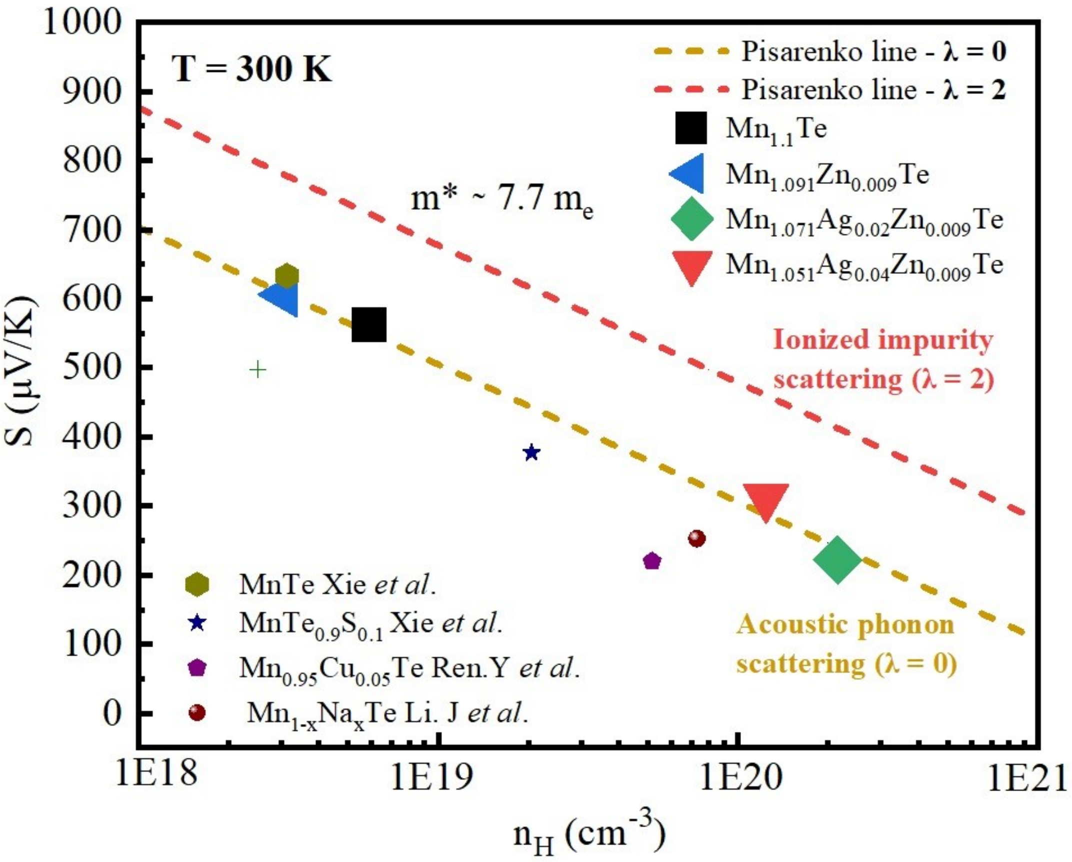

Figure S12: *Pisarenko analysis of* $Mn_{1.1}Te$, $Mn_{1.091}Zn_{0.009}Te$, $Mn_{1.071}Ag_{0.02}Zn_{0.009}Te$, *and* $Mn_{1.051}Ag_{0.04}Zn_{0.009}Te$ *samples, evaluated under both acoustic phonon and ionized impurity scattering assumptions, along with comparison to literature data.*[18,19]

Repeatability of the Sample

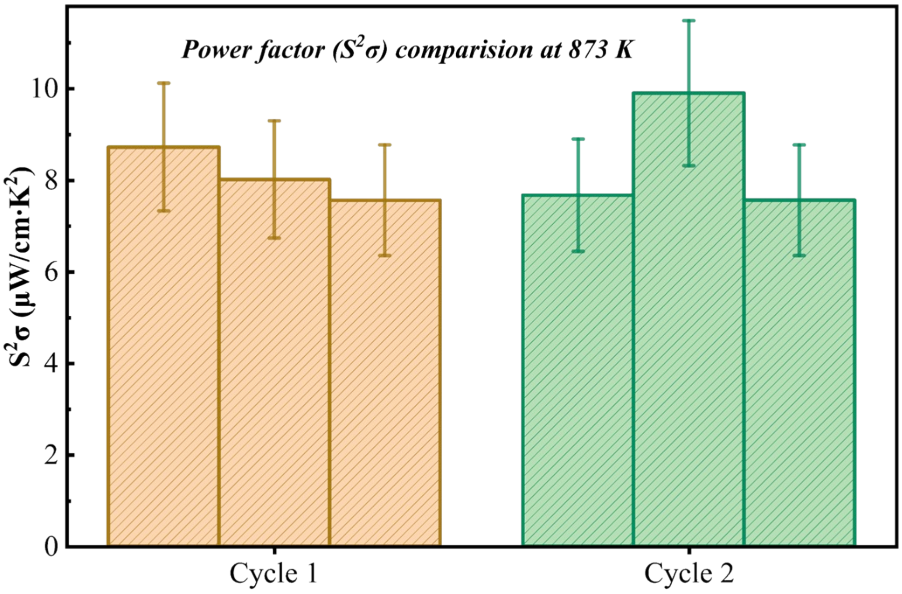

Figure S13: *Power factor comparison at 873 K for the* $Mn_{1.071}Ag_{0.02}Zn_{0.009}Te$ *sample, where Cycle 1 corresponds to the initial measurement and Cycle 2 represents the remeasurement after 42 days. The power factor values obtained in both cycles are in good agreement and fall within the experimental error limits, indicating the long-term stability and reliability of the sample.*

References

1 M. Fujikane, K. Kurosaki, H. Muta and S. Yamanaka, *J. Alloys Compd.*, 2005, **393**, 299–301.

2 A. R. Muchtar, B. Srinivasan, S. Le Tonquesse, S. Singh, N. Soelami, B. Yuliarto, D. Berthebaud and T. Mori, *Adv. Energy Mater.*, 2021, **11**, 2101122.

3 D. G. Cahill, S. K. Watson and R. O. Pohl, *Phys. Rev. B*, 1992, **46**, 6131-6144.

4 J. Dong, F. H. Sun, H. Tang, K. Hayashi, H. Li, P. P. Shang, Y. Miyazaki and J. F. Li, *ACS Appl. Mater. Interfaces*, 2019, **11**, 28221–28227.

5 C. L. Wan, W. Pan, Q. Xu, Y. X. Qin, J. D. Wang, Z. X. Qu and M. H. Fang, *Phys. Rev. B*, 2006, **74**, 144109.

6 V. P. Kannan, V. Lourdhusamy, I. Paulraj, S. Madanagurusamy and C. J. Liu, *ACS Appl. Mater. Interfaces*, 2024, **16**, 58677–58688.

7 G. A. Slack, S. Galginaitis, M. R. Lorenz, R. E. Halsted, W. E. Medcalf, R. H. Fahrig, R. Juza, A. Rabenau and G. Pascher, *J. Phys. Chem. Solids*, 1958, **1**, 89–95.

8 S. S. S. Gadhavajhala, V. P. Kannan, A. J. Kale, R. Batra, S. R. Mishra and B. Srinivasan, *Small*, 2025, **21**, 2411481.

9 J. Xin, J. Yang, Q. Jiang, S. Li, A. Basit, H. Hu, Q. Long, S. Li and X. Li, *Nano Energy*, 2019, **57**, 703–710.

10 R. Hanus, M. T. Agne, A. J. E. Rettie, Z. Chen, G. Tan, D. Y. Chung, M. G. Kanatzidis, Y. Pei, P. W. Voorhees and G. J. Snyder, *Adv. Mater.*, 2019, **31**, 1900108.

11 S. Gahlawat, R. He, S. Chen, L. Wheeler, Z. F. Ren and K. W. White, *J. Appl. Phys.*, 2014, **116**, 083516.

12 S. R. Mobasser and T. R. Hart, *Proc. Int. Conf. Light Scatt. Solids*, 1975, 202–206.

13 J. P. Perdew, K. Burke and M. Ernzerhof, *Phys. Rev. Lett.*, 1996, **77**, 3865–3868.

14 K. Koepernik and H. Eschrig, *Phys. Rev. B*, 1999, **59**, 1743-1757.

15 D. Kriegner, H. Reichlova, J. Grenzer, W. Schmidt, E. Ressouche, J. Godinho, T. Wagner, S. Y. Martin, A. B. Shick, V. V. Volobuev, G. Springholz, V. Holý, J. Wunderlich, T. Jungwirth and K. Výborný, *Phys. Rev. B,* 2017, **96**, 214418.

16 A. Basit, J. Xin, Y. Luo, J. Y. Y. Dai and J. Yang, *Adv. Electron. Mater.*, 2024, **10**, 2300809.

17 S. Rooj, J. Chakraborty and N. Ganguli, *Adv. Phys. Res.*, 2024, **3**, 2300050.

18 W. Xie, S. Populoh, K. Gałązka, X. Xiao, L. Sagarna, Y. Liu, M. Trottmann, J. He and A. Weidenkaff, *J. Appl. Phys.*, 2014, **115**, 103707.

19 Y. Xu, W. Li, C. Wang, J. Li, Z. Chen, S. Lin, Y. Chen and Y. Pei, *J. Mater. Chem. A*, 2017, **5**, 19143–19150.